Predictions of thermal and gravitational signals of Jupiter's deep zonal winds

Junjun Liu [a,*], Tapio Schneider [a], Yohai Kaspi [b]

[a] California Institute of Technology, Pasadena, CA, USA
[b] Weizmann Institute of Science, Rehovot, Israel

ARTICLE INFO

ABSTRACT

NASA's Juno spacecraft will make microwave and gravity measurements of Jupiter. These can reveal information about the composition of Jupiter's atmosphere and about the temperature and density structure below the visible clouds, which is in balance with the structure of the zonal winds. Here we show that there exist strong physical constraints on the structure of the off-equatorial deep zonal winds, and that these imply dynamical constraints on the thermal and gravitational signals Juno will measure. The constraints derive from the facts that Jupiter is rapidly rotating, has nearly inviscid flow, and has strong intrinsic heat fluxes emanating from the deep interior. Because of the strong intrinsic heat fluxes, Jupiter's interior is convecting, but the rapid rotation and weak viscosity constrain the convective motions away from the equator to occur primarily along cylinders parallel to the planet's spin axis. As a consequence, convection is expected to approximately homogenize entropy along the spin axis, thereby adjusting the interior to a convectively and inertially nearly neutral state. In this state, entropy gradients perpendicular to the spin axis are constant but generally not zero on cylinders concentric with the spin axis. Additionally, thermal wind balance relates entropy gradients perpendicular to the spin axis to the zonal wind shear between the observed cloud-level winds and winds in the deep interior (pressures of order 10^6 bar), which must be much weaker because otherwise the Ohmic energy dissipation produced by the interaction of the zonal winds with the planetary magnetic field would exceed the planetary luminosity. Combining these physical constraints with thermal and electrical properties of the atmosphere, we obtain that zonal winds away from the equator likely extend deeply into Jupiter (to a depth between about $0.84R_J$ and $0.94R_J$ with Jupiter radius R_J) but have strengths similar to cloud level winds only within the outer few percent of Jupiter's radius. Meridional equator-to-pole temperature contrasts in thermal wind balance with the zonal winds increase with depth and reach $\sim$1–2 K at 50 bar; they would reach $O(10\,\mathrm{K})$ if the winds were shallowly confined, as has been proposed previously. Such temperature contrasts will be detectable by Juno's microwave instrument and are expected to be much larger than those associated with variations in water vapor abundance. The associated gravitational signals of the zonal winds will also be detectable by Juno, but they will be more difficult to distinguish from those implied by other flow models with deep zonal flows. The combination of Juno's gravity and microwave instruments should be able to distinguish deep flows (detectable gravitational signals) from shallow flows (detectable thermal signals), providing strong constraints on the penetration depth of substantial zonal winds.

© 2013 Elsevier Inc. All rights reserved.

1. Introduction

The only available data about the zonal wind, temperature, and density of Jupiter below the visible clouds come from the descent of the Galileo probe into the planet in 1995, delivering data about the atmosphere at the entry point (6.5°N) up to pressures of ~21 bar (Atkinson et al., 1997, 1998). NASA's Juno mission will reach Jupiter in 2016 and is expected to deliver the first data set of the temperature and density structure below the visible clouds.

It will make microwave and gravity measurements from orbit around Jupiter. These measurements will contain information about the composition of the atmosphere (which affects emissivities and the equation of state) and about the flow (which affects temperature and density gradients). To disentangle compositional and dynamical information, it is essential to have independent constraints on either. Here we show that there exist strong dynamical constraints on the density and temperature structure, and we calculate the gravity and temperature signals they imply under plausible assumptions for free parameters in the flow structure.

The dynamical constraints derive from the well known facts that Jupiter is rapidly rotating, has strong intrinsic heat fluxes emanating from the deep interior, and has nearly inviscid flow

---

* Corresponding author. Address: California Institute of Technology, Mail Code 131-24, 1200 E. California Blvd., Pasadena, CA 91125, USA.
E-mail address: ljj@gps.caltech.edu (J. Liu).

(Ingersoll et al., 2004; Guillot et al., 2004). The intrinsic heat flux ($\sim$6 W m^{-2}) is sufficiently strong to lead to convection in Jupiter's deep interior, up to near the tropopause (Guillot, 1999). Convective plumes penetrating into the upper troposphere have indeed been observed (Gierasch et al., 2000; Porco et al., 2003; Sánchez-Lavega et al., 2008). Jupiter's rapid planetary rotation (small Rossby numbers) and negligible viscosity imply that convective motions are predominantly confined to surfaces of constant angular momentum per unit mass (Busse, 1976, 1994; Christensen, 2001; Heimpel et al., 2005; Aurnou et al., 2008; Kaspi et al., 2009; Jones and Kuzanyan, 2009; Gastine and Wicht, 2012). These angular momentum surfaces are approximately cylinders concentric with the planet's spin axis because the small Rossby number means the angular momentum is dominated by the contribution from the planetary rotation. Because viscous dissipation is negligible in Jupiter's atmosphere and radiative adjustment timescales below the upper troposphere are longer than convective timescales (Guillot et al., 2004; Guillot, 2005), we expect that, in the interior, entropy is approximately materially conserved in convective motions and so will become approximately homogenized along angular momentum surfaces. That is, we expect that convection homogenizes entropy in the direction of the planet's spin axis, establishing a state that is nearly neutral with respect to convective and inertial instabilities, in which entropy and angular momentum surfaces are aligned (Emanuel, 1983, 1994; Thorpe and Rotunno, 1989). Indeed, data from the descent of the Galileo probe show that the stratification of the atmosphere below the clouds is close to convectively neutral (Magalhães et al., 2002). But because the rapid planetary rotation constrains motion perpendicular to angular momentum surfaces to be weak, entropy need not be approximately homogenized perpendicular to the spin axis—a restrictive assumption that has often been made in models of Jupiter's interior (e.g., Ingersoll and Porco, 1978), but that, as we will discuss, is unlikely to be satisfied for dynamical reasons (Liu and Schneider, 2010). Instead, entropy homogenization along the spin axis implies that entropy gradients perpendicular to the spin axis are constant along cylinders—a less restrictive assumption that we will exploit to constrain the flow structures at depth.

Entropy gradients perpendicular to the spin axis are related to the zonal wind and its shear through the thermal wind balance (Smith et al., 1982; Vallis, 2006; Kaspi et al., 2009). The zonal wind shear below the visible clouds is not generally known (except in the upper layers of the atmosphere and at the Galileo entry site); however, the zonal wind at the cloud level is known (Limaye, 1986; Porco et al., 2003). It is very unlikely that the zonal winds extend into the deep interior unabatedly because if they would, their interaction with the planetary magnetic field would generate electric currents deep in the interior, where the atmosphere is electrically conducting (Nellis et al., 1996). The Ohmic energy dissipation of these electric currents (and thus ultimately the dissipation of kinetic energy) would exceed the net planetary luminosity (Liu et al., 2008). This is impossible since the kinetic energy dissipation cannot exceed the total energy available to drive the flow from intrinsic heat fluxes and absorption of solar energy combined. Liu et al. (2008) showed that at 0.96R_J (Jupiter radius R_J), the zonal winds must be weaker than the observed upper-tropospheric winds for the Ohmic dissipation to be smaller than the net planetary luminosity.

The notion that zonal winds in Jupiter's interior are much weaker than at cloud level is supported by recent numerical simulations that take a radially varying electrical conductivity into account and that show slow convection in the dynamo region (with higher electrical conductivity) coexisting with strong zonal flows higher up in the atmosphere (Heimpel and Gómez Pérez, 2011). It is also supported by measurements of the secular variation of Jupiter's magnetic field, which suggest flow velocities of order of 10^{-3} m s^{-1} in

the planetary interior (Russell et al., 2001; Guillot et al., 2004). So the zonal wind shear is constrained by observations of the winds at cloud level, by the thermal wind balance, by the assumption of entropy gradients perpendicular to the spin axis being constant along cylinders, and by the requirement that the winds at depth are negligibly weak compared with the cloud-level winds. We will exploit these constraints to make predictions of the thermal and gravitational signals of Jupiter's deep zonal winds, assuming a fixed composition (equation of state) of the atmosphere.

Section 2 begins with a review of thermal wind balance in a deep atmosphere and calculates the temperature structure implied by the zonal winds, under different assumptions about the level at which they are negligibly weak. Section 3 calculates the gravitational signals implied by the zonal winds. Section 4 summarizes the results and implications for measurements by the Juno mission.

2. Thermal signals of deep zonal winds

2.1. Thermal wind balance in a deep atmosphere

Jupiter's rapid rotation means that the Rossby number Ro = $U/(2\Omega L_\perp)$ is small (with zonal velocity scale U, angular velocity of planetary rotation Ω, and length scale of zonal-flow variations $L_\perp$ in the direction perpendicular to the planet's spin axis). With typical scales for upper-tropospheric zonal winds ($U \lesssim 100$ m s^{-1}, $L_\perp \sim 2000$ km), the Rossby number is $\lesssim$0.1, and it is even smaller for the weaker zonal winds expected in the planetary interior (Schneider and Liu, 2009). Additionally, viscous and other momentum dissipation is expected to be weak (small Ekman number) above any dissipative layer at depth, e.g., where the interaction of magnetic fields with flows generates dissipation. Therefore, the atmospheric flow above any dissipative layer at depth is expected to be in geostrophic balance to leading order, and to the extent the atmosphere is also in hydrostatic balance, thermal wind balance holds. For a deep atmosphere (i.e., not making the thin-shell approximation), the thermal wind balance in the anelastic approximation is (Ingersoll and Pollard, 1982; Kaspi et al., 2009)

$$2\mathbf{\Omega} \cdot \nabla \mathbf{u} - 2\Omega \nabla \cdot \mathbf{u} = \alpha_s \nabla s' \times \mathbf{g}. \tag{1}$$

Here, $\mathbf{\Omega}$ is the planetary angular velocity vector, $\mathbf{u}$ is the 3D atmospheric velocity vector, $\mathbf{g}(r)$ is the gravitational acceleration, and s is the specific entropy; primes denote fluctuations about a reference state with constant entropy $\tilde{s}$ and with hydrostatically balanced pressure $\tilde{p}(r)$ and density $\tilde{\rho}(r)$

$$\nabla \tilde{p}(r) = \tilde{\rho}(r)\mathbf{g}(r), \tag{2}$$

where r is the spherical radius. (We neglect Jupiter's oblateness throughout this paper. The gravitational acceleration $\mathbf{g}(r)$ depends on the density $\tilde{\rho}(r)$ in the hydrostatic reference state and varies with r.) The coefficient

$$\alpha_s = -\frac{1}{\tilde{\rho}} \left(\frac{\partial \rho}{\partial s} \right)_p \tag{3}$$

is an entropic expansion coefficient that relates isobaric density fluctuations to entropy fluctuations (i.e., $\rho'/\tilde{\rho} = -\alpha_s s'$ at $p' = 0$); for an ideal gas, $\alpha_s = 1/c_p$, where c_p is the specific heat capacity at constant pressure. Because of the generally nonzero baroclinic term $\alpha_s \nabla s' \times \mathbf{g}$ on the right hand side of the thermal wind Eq. (1), the Taylor–Proudman theorem does not necessarily apply, although both the Rossby and Ekman numbers are small in Jupiter's off-equatorial region (Pedlosky, 1987). Instead of the homogenized entropy and vanishing zonal wind shear along the spin axis under Taylor–Proudman conditions, the zonal wind shear along the spin axis and the corresponding entropy perturbations perpendicular to it

are not necessarily small on Jupiter but are related by the thermal wind equation and are coupled dynamically through a mean meridional circulation (Schneider and Liu, 2009).

For our purposes, it is convenient to use cylindrical coordinates (with cylindrical radius $r_\perp$ and height z above the equatorial plane measured in the direction of the planet's spin axis), and to focus on the zonal (azimuthal) wind component u. Thermal wind balance then becomes

$$2\Omega \frac{\partial u}{\partial z} = \alpha_s g \sin \phi \frac{\partial s'}{\partial r_\perp} - \alpha_s g \cos \phi \frac{\partial s'}{\partial z}, \tag{4}$$

where ϕ is latitude, related to the cylindrical coordinates through

$$\sin \phi(z, r_\perp) = \frac{z}{(z^2 + r_\perp^2)^{1/2}}. \tag{5}$$

This thermal wind equation relates the zonal wind shear along the spin axis to the entropy variations in Jupiter's deep atmosphere; it generalizes the standard thermal wind equation for an ideal-gas atmosphere in a thin shell (e.g., Ingersoll and Cuzzi, 1969).[1]

The observed intrinsic heat flux emanating from Jupiter's deep interior is so strong that, in the interior, heat is transferred primarily by convection (Guillot et al., 2004). This convection is expected to be sufficiently vigorous to homogenize entropy along the direction of convective motions (Guillot and Morel, 1995; Guillot, 2005). Because the Rossby number is small and viscous momentum dissipation and thermal diffusion are negligible, convective motions are approximately aligned with surfaces of constant planetary angular momentum, which are cylinders concentric with the planet's spin axis (Busse, 1976; Aurnou et al., 2008; Kaspi et al., 2009). Therefore, where solar radiative fluxes are sufficiently weak and thermal radiative adjustment timescales are sufficiently large (below the upper troposphere), convection tends to homogenize entropy in the direction of—but not necessarily perpendicular to—the planet's spin axis. The radiative-convective equilibrium state with entropy homogenized along angular momentum surfaces is neutral with respect to convective and inertial axisymmetric instabilities and has zero slantwise convective available potential energy, which convection tends to deplete (Emanuel, 1994; Thorpe and Rotunno, 1989). The tendency of convection to homogenize entropy in the direction of the spin axis ($\partial s'/\partial z \ll \partial s'/\partial r_\perp$) means that the thermal wind balance (4) reduces to

$$\frac{\partial u}{\partial z} \approx \frac{\alpha_s g \sin \phi(z, r_\perp)}{2\Omega} \frac{\partial s'}{\partial r_\perp}. \tag{7}$$

This relates entropy gradients perpendicular to the spin axis to the zonal velocity shear along the spin axis. Evidence that this is in fact the dominant balance comes, for example, from the general circulation model simulations of Jupiter's upper atmosphere in Schneider and Liu (2009) and Liu and Schneider (2010), which have radiative and intrinsic energy fluxes consistent with Jupiter observations and equilibrate to a statistically steady state with entropy approximately homogenized along angular momentum surfaces below ∼0.7 bar and away from the equator. At deeper levels in the simulations, the meridional entropy gradient (the thin-shell analog of $\partial s'/\partial r_\perp$) varies with latitude, and the vertical entropy gradient is about an order of magnitude smaller than the meridional entropy gradient. Within a few degrees of the equator, this is not necessarily true, as the Rossby number may not be small and the thermal wind equation does not hold accurately (Aurnou et al., 2008); however, our focus here is on the off-equatorial regions. Additionally, simulations of deeper atmospheric shells show that thermal plumes away from the equatorial region indeed generally align with the planet's spin axis and that the dominant component of the convective heat transfer is axial (Aurnou et al., 2008; Kaspi et al., 2009).[2]

2.2. Constraints on the depth of zonal winds and on entropy gradients

The thermal wind balance (7) shows how a given zonal wind shear along the spin axis is associated with an entropy gradient perpendicular to the spin axis. The zonal wind shear is related to the penetration depth of substantial zonal winds. If the zonal winds are confined to a shallow weather layer (e.g., Ingersoll et al., 2004), the zonal wind shear along the spin axis and the associated entropy gradient perpendicular to it are large. If the zonal winds penetrate deeply (e.g., Busse, 1994), the zonal wind shear along the spin axis and the associated entropy gradient perpendicular to it are smaller.

Within the atmospheric shell with substantial zonal winds, the zonal winds are almost certainly sheared in the direction of the spin axis, and the associated entropy gradients perpendicular to the spin axis are nonzero. The reason is that the zonal winds and entropy gradients must satisfy two constraints: (i) they must be approximately in thermal wind balance where dissipation is weak and (ii) along any angular momentum surface (approximately a cylinder), the net angular momentum flux convergence by eddies must be balanced by angular momentum dissipation at depth (Schneider and Liu, 2009; Liu and Schneider, 2010). These twin constraints generally cannot be satisfied with zonal winds that do not vary in the direction of the spin axis. Rather, zonal winds generally must be sheared along angular momentum surfaces, as seen in the simulations in Schneider and Liu (2009) and Kaspi et al. (2009). The Taylor–Proudman state, in which entropy is completely homogenized and the zonal winds are constant along the spin axis, is unlikely to be attained in the atmospheric shell of substantial zonal winds.

For Jupiter, observations of the flow in the upper troposphere provide constraints on the depth to which substantial zonal winds can extend. It has been observed that in the upper troposphere, eddies generally transport angular momentum out of retrograde and into prograde jets, thus transferring kinetic energy to the mean zonal winds (Ingersoll et al., 1981; Salyk et al., 2006). It is not clear how deeply into the atmosphere this kinetic energy transfer extends. But if the eddy angular momentum fluxes per unit volume extended unabatedly over a layer of only 50 km thickness (e.g., from about 0.3 to 2.5 bar pressure) and if vertical zonal-wind variations over this layer are weak (as is generally assumed), the total energy conversion rate would already amount to 0.5 W m^{-2}, or ∼4% of the total energy uptake of the atmosphere from intrinsic heat fluxes and absorption of solar radiation. It would be

---

[1] The thermal wind equation reduces to the standard thermal wind equation for an ideal-gas atmosphere ($s' = c_p \log \theta$ with potential temperature θ) in the limit of a thin atmospheric shell ($r = a = $ const., neglecting vertical Coriolis accelerations),

$$\frac{\partial u}{\partial \bar{z}} = -\frac{g}{f \theta} \frac{\partial \theta}{\partial y}. \tag{6}$$

Here, $y = a\phi$ is the meridional coordinate, $\bar{z}$ is the altitude (spherical radius) coordinate (with $\bar{z} \sin \phi = z$ and $\bar{z} \cos \phi = r_\perp$), and $f = 2\Omega \sin \phi$ is the Coriolis parameter.

[2] Simulations of deeper atmospheric flows on Jupiter generally use excessive isotropic viscous dissipation of momentum and entropy throughout the interior, rather than dissipation solely at depth. As a result, they exhibit a tendency toward isotropic entropy homogenization (e.g., Aurnou et al., 2008; Jones and Kuzanyan, 2009). Zonal winds and the associated thermal wind shear do not satisfy the constraints discussed in Section 2.2 in a way that is consistent with the angular momentum fluxes observed in the upper troposphere, which for energetic reasons must be baroclinic and cannot extend to great depths (Schneider and Liu, 2009; Liu and Schneider, 2010). Therefore, it is difficult to infer relative magnitudes of entropy gradients in the direction of the spin axis and perpendicular to it from such simulations.

correspondingly larger or smaller if the angular momentum fluxes were confined to a deeper or shallower layer (Liu and Schneider, 2010). Therefore, the kinetic energy transfer from eddies to the mean flow must be baroclinic and cannot extend to great depths. In a statistically steady state, mean-flow kinetic energy must either be dissipated at depth at a rate equal to the upper-tropospheric transfer from eddies or must be transferred back to eddies by angular momentum fluxes opposing those observed in the upper troposphere. It is very unlikely that there are eddy angular momentum fluxes at depth that exactly balance those in the upper troposphere; no model has produced such angular momentum fluxes, and no mechanisms to generate them have been proposed. So the mean zonal winds likely experience dissipation at depth. A plausible dissipation mechanism is the magnetohydrodynamic (MHD) drag that is produced by the interaction of winds with the magnetic field and the Ohmic dissipation of the resulting electric currents. This occurs at depths where the electrical conductivity of the atmosphere is sufficiently large.

The electrical conductivity of hydrogen (Jupiter's main constituent) can be calculated using a semiconductor model with linear band gaps determined by experimental shockwave data (Nellis et al., 1992, 1996; Liu et al., 2008). The derived electrical conductivity increases exponentially with depth up to a plateau at $\sim 0.84 R_J$, where it reaches 2×10^5 S m^{-1} (Fig. 1a). Above $0.94 R_J$, it is in agreement with the electrical conductivity determined by ab initio simulations (French et al., 2012). Below $0.94 R_J$, the electrical conductivity determined by ab initio simulations increases more rapidly with depth and reaches 3.39×10^6 S m^{-1} at around $0.1 R_J$ (Fig. 1a). For the inferences in this paper, we will primarily use the electrical conductivity calculated from the semiconductor model but will discuss results implied by the electrical conductivity determined from ab initio simulations where applicable.

The Ohmic dissipation produced by the interaction of a given magnetic field with the zonal winds scales linearly with electrical conductivity (Liu, 2006; Liu et al., 2008). At $\sim 0.84 R_J$, zonal winds on the order of 10^{-2} m s^{-1} would already experience a substantial dissipation of more than 1 W m^{-2} (assuming the magnetic field can be obtained by downward continuation of the upper atmospheric field; see Appendix A). So the zonal winds likely are negligibly weak at this and deeper levels (Liu, 2006). On the other hand, outside $\sim 0.97 R_J$, the electrical conductivity is so low ($\lesssim 10^{-3}$ S m^{-1}) that zonal winds of the strength of those observed in the upper troposphere would experience less than 10^{-2} W m^{-2} dissipation— about an order of magnitude less than the total dissipation in the simulation in Schneider and Liu (2009). So substantial zonal winds likely extend to deeper levels. Hence, the Ohmic dissipation produced by interaction with the magnetic field constrains substantial zonal winds to extend to a cutoff radius r_c that lies somewhere between $0.84 R_J$ and $0.97 R_J$, corresponding to between about 1.4×10^6 and 3.6×10^4 bar pressure. Because the electrical conductivity increases exponentially with depth, this constraint on the cutoff radius is not very sensitive to uncertainties about the strength of the magnetic field (which increases with depth, toward the source of the field). For example, a magnetic field an order of magnitude stronger than that at the top of Jupiter's atmosphere would increase the lower bound on r_c to $0.89 R_J$ (see Appendix A).

The Ohmic dissipation constraint derives from the energy balance. Additional constraints derive from the angular momentum and hydrostatic balance, which allow us to tighten the upper bound of the depth range to which substantial zonal winds may extend. At levels below the cutoff radius, either thermal wind balance has to break down or entropy must be isotropically homogenized, so that the zonal winds can remain weak at these deeper levels. (Otherwise, thermal wind balance and constant entropy gradients perpendicular to the spin axis would continue to imply shear in the direction of the spin axis, implying a reversal and strengthening of zonal winds that would violate the energetic constraints.) Thermal wind balance breaks down where the electrical conductivity is sufficiently large that the Maxwell stress determines the zonal wind shear along the spin axis. Order-of-magnitude
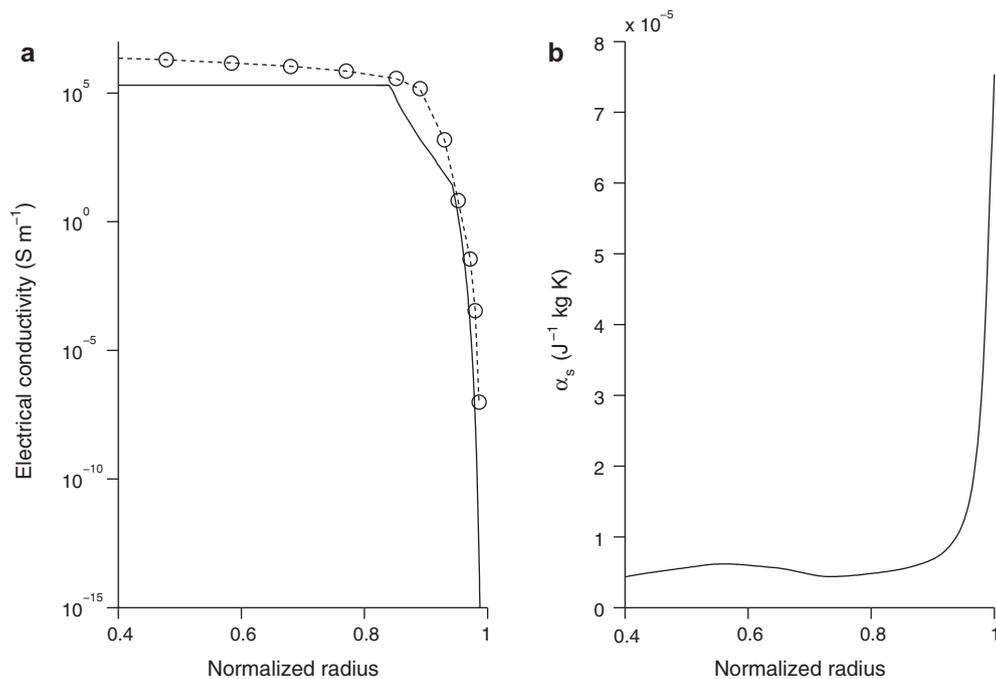

Fig. 1. (a) Electrical conductivity profile as a function of normalized radius. The solid line is from the semiconductor model with linear band gaps determined by experimental shockwave data (Nellis et al., 1992, 1996; Liu et al., 2008). From $0.94 R_J$ to the top of the atmosphere, the electrical conductivity is obtained from Liu et al. (2008); below $0.94 R_J$, the electrical conductivity is adapted from Nellis et al. (1996). (See Nellis et al. (1992, 1996) and Liu (2006) for discussion of uncertainties.) The dashed line with circles is the electrical conductivity along Jupiter's adiabat determined by ab initio simulations (French et al., 2012). (b) Entropic expansion coefficient α_s as function of normalized radius for the SCVH EOS.

estimates indicate that the Maxwell stress starts to become important at or below ~$0.94R_J$ (see Appendix B). So assuming that radiative fluxes are too weak to isotropically homogenize entropy outside ~$0.94R_J$, it is unlikely that the cutoff radius for substantial zonal winds is larger than that. Therefore, as a conservative bracket for the cutoff radius, we assume it is in the range of 0.84 to $0.94R_J$, corresponding to 1.4 to 0.2 Mbar pressure. Additionally, calculations using the electrical conductivity profile from ab initio simulations (French et al., 2012) do not change the $0.94R_J$ upper bound but likewise move the lower bound to $0.89R_J$ because the electrical conductivity below $0.94R_J$ in the ab initio simulations is significantly higher than that derived by simple semiconductor models (Fig. 1a).

2.3. Possible zonal winds and entropy gradients

Integrating the thermal wind Eq. (7) along the planet's spin axis from the cylindrical depth $z_c = z_c(r_c, r_\perp)$ corresponding to the spherical cutoff radius r_c (where $u \approx 0$) to the upper troposphere at cylindrical depth $z_R = z_R(R, r_\perp)$ and spherical radius R gives a relation between the upper-tropospheric zonal wind $u_R(\phi) = u_R(r_\perp(\phi))$ and the thermal structure of the atmosphere below:

$$u_R(\phi) = \frac{1}{2\Omega} \frac{\partial s'}{\partial r_\perp} \int_{z_c}^{z_R} \alpha_s g \sin \phi' \, dz. \tag{8}$$

Here, $\sin \phi' = z/(z^2 + r_\perp^2)^{1/2}$, and the entropy gradient $\partial s'/\partial r_\perp$ perpendicular to the spin axis can be taken outside the integral because the assumption that entropy is homogenized along the spin axis implies that the gradient perpendicular to it must be constant going down along the spin axis. Solving for this gradient gives

$$\frac{\partial s'}{\partial r_\perp} = \frac{2\Omega u_R(\phi)}{\int_{z_c}^{z_R} \alpha_s g \sin \phi' \, dz}, \tag{9}$$

which relates it to the observed upper-tropospheric zonal winds u_R, the cutoff-radius r_c, and the entropic expansion coefficient α_s.

To determine the entropic expansion coefficient α_s, an equation of state (EOS) is needed. In Jupiter's upper atmosphere, the EOS is well approximated by that for an ideal gas. Deep in the interior, as the pressure and temperature increase, hydrogen becomes semiconducting because of the effects of pressure ionization, electron degeneracy, and Coulomb interactions. There, the EOS differs from that for an ideal gas. We use the Saumon–Chabrier–Van Horn (SCVH) EOS (Saumon et al., 1995) with the reference entropy measured by the Galileo probe, following Kaspi et al. (2009) who applied this EOS in Jupiter simulations.[3] This adiabatic reference profile matches well with the modeled interior mean density–temperature–pressure profile (Guillot and Morel, 1995), although differences exist (Kaspi et al., 2009). In using the SCVH EOS, we ignore the effects of latent heat release in phase transitions (e.g., of water) on the entropy. Fig. 1b shows the resulting entropic expansion coefficient α_s as a function of the normalized radius. It rapidly decreases with depth, in part because the mean density in the denominator of (3) increases rapidly with depth.

The rapid decrease of α_s with depth means that, by thermal wind balance (7) and using $\partial s'/\partial r_\perp \approx$ const, most of the zonal wind shear will be concentrated in the outer few percent of Jupiter's radius, irrespective of where substantial dissipation occurs (see Fig. 2 for an illustration). Thus, the value of the entropy gradient perpen-

---

dicular to the spin axis (9) is not very sensitive to the chosen cutoff radius, provided it is sufficiently small so that it lies below the layer of substantial α_s (cf. Fig. 1b). Whether $r_c = 0.9R_J$ or $r_c = 0.84R_J$ is used changes the integral $\int_{z_c}^{z_R} \alpha_s g \sin \phi' \, dz$ by less than 15% when cylinders intersecting midlatitudes in the upper troposphere are considered. The corresponding change in the entropy gradient perpendicular to the spin axis (9) likewise is less than 15%.

These expectations are borne out more precisely by calculations of the entropy gradient perpendicular to the spin axis (9) for different cutoff radii r_c. Instead of showing the entropy gradient directly as a function of $r_\perp$, we use latitude in the upper troposphere as an equivalent but more intuitive abscissa (Fig. 3a). As expected, entropy gradients corresponding to shallowly confined zonal winds are larger than those corresponding to deeply penetrating zonal winds. Moreover, since α_s is positive, going downward in the direction of the spin axis (i.e., going toward lower $|z|$ at fixed $r_\perp$), the entropy gradient $\partial s'/\partial r_\perp$ has the same sign as the upper-tropospheric zonal wind: Going downward in the direction of the spin axis where the observed zonal wind is prograde, the entropy gradient $\partial s'/\partial r_\perp$ is positive, so the entropy increases with $r_\perp$; the opposite holds where the observed zonal wind is retrograde. The entropy gradient vanishes going downward from where the observed zonal wind vanishes (Fig. 2). Thus, the correlations between the signs of the entropy gradient and of the zonal winds project downward along the spin axis.

In the equatorial region where the cylindrical radius $r_\perp$ is greater than the cutoff radius r_c (outside the tangent cylinder), the zonal wind shear in the direction of the spin axis and the entropy gradient perpendicular to it are not well constrained by the arguments we presented. Zonal winds within that region still connect with the flow at depth along surfaces of constant angular momentum per unit mass, which are approximately cylinders concentric with the spin axis. But these cylinders no longer intersect a region of substantial MHD drag. The arguments we presented hence do not constrain the zonal wind shear and the entropy gradient in that region (corresponding to latitudes $|\phi| < \arccos(r_c)$ in the upper troposphere); we have left their values open in Figs. 2 and 3. It is possible that the zonal wind shear in the direction of the spin axis and the entropy gradient perpendicular to it approximately vanish in this region, so that a Taylor–Proudman state is attained (or nearly so).

Where the zonal wind shear and entropy gradients are constrained, the zonal wind in the entire troposphere can be calculated by integrating the thermal wind balance (7) downward from the observed upper-tropospheric winds. Substituting the expression for the entropy gradient (9) into the thermal wind balance, using $u(z_c) \approx 0$, and integrating gives

$$u(z) = u_R(\phi) \frac{\int_{z_c}^{z} \alpha_s g \sin \phi' \, dz}{\int_{z_c}^{z_R} \alpha_s g \sin \phi' \, dz}. \tag{10}$$

This shows explicitly that the zonal winds under our assumptions (principally, that entropy is homogenized in the direction of the spin axis but not necessarily perpendicular to it) only depend on the cutoff-radius r_c and the EOS, which determines α_s. It provides a more physically plausible zonal wind structure than those assumed in previous models (e.g., Busse, 1976; Jones and Kuzanyan, 2009), which are difficult to reconcile with observations, for example, of angular momentum fluxes in the upper troposphere (Schneider and Liu, 2009; Liu and Schneider, 2010).

The zonal winds shown in Fig. 2 are calculated from (10) for $r_c = 0.84R_J$. The figure shows that, consistent with the preceding discussion, substantial zonal winds are primarily confined to the upper atmosphere (because of the decrease of α_s with depth). Generally, the strength both of prograde and retrograde jets decreases with depth toward zero at the cutoff radius r_c; zeros of the zonal winds project downward along the spin axis (Schneider and Liu, 2009).

---

[3] The Galileo probe measured an approximately dry adiabatic temperature–pressure profile, passing through 260 K and 4.18 bar (Seiff et al., 1998). Based on the SCVH EOS, the corresponding specific entropy is 6.27×10^4 J kg^{-1} K^{-1}. The are uncertainties about this reference entropy: it may range from 6.24 to 6.31×10^4 J kg^{-1} K^{-1} (Seiff et al., 1998). But these uncertainties about the reference entropy will only affect the mean entropy, not the meridional entropy gradients and associated temperature gradients that are our focus.
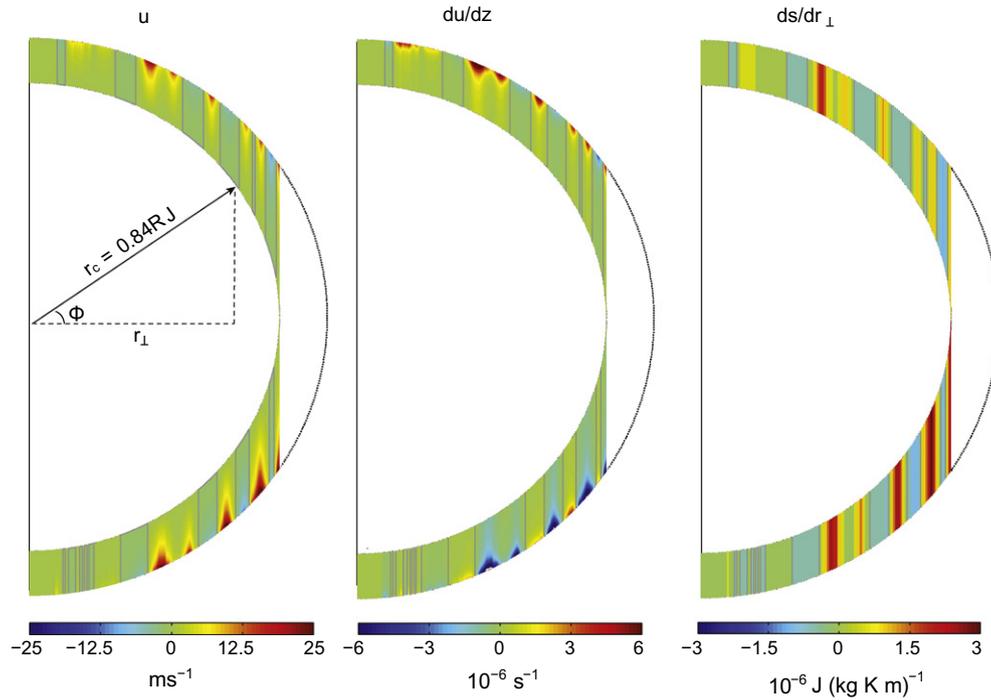
Fig. 2. Mean zonal wind u (left), its shear $\partial u/\partial z$ in the direction of the spin axis (middle), and corresponding entropy gradient perpendicular to the spin axis $\partial s'/\partial r_\perp$ (right), all for a cutoff radius $r_c = 0.84R_J$. The gray contours indicate the zero lines.
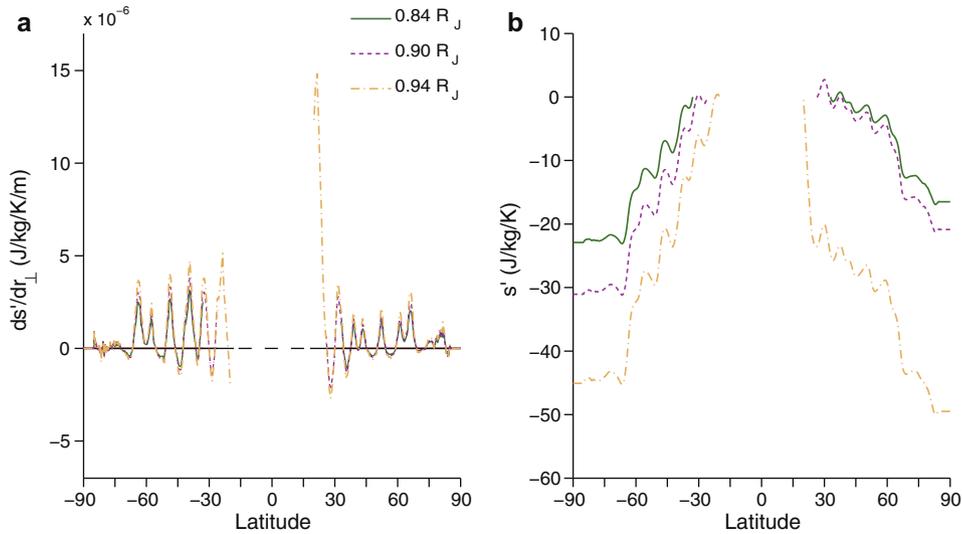

Fig. 3. (a) Entropy gradient $\partial s'/\partial r_\perp$ perpendicular to the spin axis as a function of latitude ϕ in the upper troposphere. (b) Entropy perturbation (relative to isentropic reference state) s' as a function of latitude ϕ. The integration constant to obtain the entropy perturbation was arbitrarily fixed so that $s' = 0$ at the tangent cylinder where $r_\perp = r_c$. Green solid lines correspond to $r_c = 0.84R_J$, magenta dashed lines to $r_c = 0.90R_J$, and orange dash-dot lines to $r_c = 0.94R_J$. (For interpretation of the references to color in this figure legend, the reader is referred to the web version of this article.)

2.4. Implications for temperature gradients

To obtain the entropy perturbation s' in the interior atmosphere as a function of cylindrical radius (or latitude), we integrate Eq. (9) for the entropy gradient from the pole to the tangent cylinder where $r_\perp = r_c$ (see Fig. 2), arbitrarily fixing the integration constant so that $s' = 0$ at the tangent cylinder. As is already clear from the entropy gradients, the equator-to-pole entropy contrast increases with increasing cutoff radius (Fig. 3b). For $r_c = 0.84R_J$, the equator-to-pole entropy contrast is less than 25 J kg^{-1} K^{-1}; for $r_c = 0.94$-R_J, the equator-to-pole entropy contrast is 50 J kg^{-1} K^{-1}; for the even larger cutoff radius of $r_c = 0.9965R_J$ (corresponding to a pressure of 100 bar), which we consider unrealistic, the equator-to-pole entropy contrasts would reach 475 J kg^{-1} K^{-1}. However, these entropy contrasts are still small compared with the entropy of the reference state we assumed ($\tilde{s} = 6.27 \times 10^4$ J kg^{-1} K^{-1}, see footnote 3), so the assumption in (1) of small entropy fluctuations about the reference state is well justified.

The temperatures T corresponding to the entropies s can be obtained from the EOS. Fig. 4 shows contours of pressure p as a function of $\log(s/\tilde{s})$ and $\log(T/T_0)$ (reference temperature T_0) for the SCVH EOS. The mean temperature increases with pressure in the
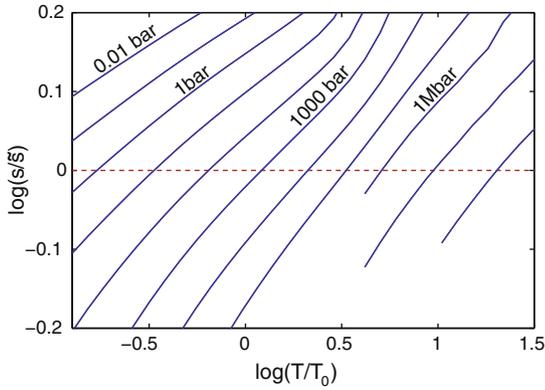
Fig. 4. Contours of pressure p as a function of $\log(s/\bar{s})$ and $\log(T/T_0)$ for the SCVH EOS (blue). The mean isentropic reference state with the entropy $\bar{s} = 6.27 \times 10^4$ J kg^{-1} K^{-1} determined by Galileo probe measurement at the entry point is shown as the red dashed horizontal line. The reference temperature for normalization is chosen to be $T_0 = 1000$ K. The first contour in the upper left corner corresponds to $p = 0.01$ bar, and pressure increases by a factor of 10 for each additional contour to the right. (For interpretation of the references to color in this figure legend, the reader is referred to the web version of this article.)

isentropic reference state, and the magnitude of temperature deviations for a given entropy deviation from the reference state also increases with pressure. For example, a 0.1% deviation of the entropy from the reference state corresponds to a 1.5-K temperature deviation at 1 bar, to a 10-K temperature deviation at 10^3 bar, and to a 20-K temperature deviation at 10^6 bar.

Fig. 5 shows the temperature perturbation as a function of latitude at different pressures and for different cutoff radii. (The temperature at the tangent cylinder is fixed by the integration constant for the perturbation entropy.) As for the entropy perturbations, the temperature perturbations are larger for shallower cutoff radii, as was recognized decades ago (e.g., Smith et al., 1982). For a cutoff radius of $0.84R_J$, the equator-to-pole temperature contrast is ~0.4 K at the 1-bar level and ~1 K at the 50-bar level. For a cutoff radius of $0.94R_J$, the equator-to-pole temperature contrast is ~0.7 K at the 1-bar level and ~2 K at the 50-bar level. For calculations with unrealistic cutoff radii of $0.9965R_J$ (corresponding to

100 bar), $0.9954R_J$ (200 bar), and $0.9917R_J$ (1000 bar), the temperature contrasts at different pressures are much larger, reaching $O(10\,\text{K})$ at 50 bar (Fig. 6).

2.5. Implications for Juno's microwave measurements

Juno's microwave instrument is designed to measure the brightness temperature in six channels that are sensitive to different pressure intervals between 0.5 bar and $O(100\,\text{bar})$. It is expected to detect relative brightness temperature variations of 0.1%, or variations of 0.1 K in a mean brightness temperature background of 100 K (Janssen et al., 2005).

According to our results, at ~10 bar with a mean brightness temperature of 330 K, plausible equator-to-pole temperature contrasts associated with the zonal winds range from ~0.6 K (for $r_c = 0.84R_J$) to ~1.2 K (for $r_c = 0.94R_J$). These dynamical temperature variations are much larger than the expected detection limit. By contrast, Janssen et al. (2005) shows that a variation in water vapor relative humidity from 100% to 20% has less than 0.1% effect on brightness temperature. Thus, the meridional temperature variations associated with the zonal winds are more easily detectable than variations of water vapor relative humidity.

However, the thermal signals produced by variations of ammonia abundances can be much larger than those produced by the zonal winds. Janssen et al. (2005) shows that increasing the ammonia abundance from 3 to 5 times solar abundance decreases the microwave brightness temperature by 20–25 K. If the ammonia abundances exhibit large meridional variations, it may be difficult to detect the temperature variations associated with the zonal winds. But if ammonia abundances are meridionally homogenized at depth, Juno's microwave measurements, if they indeed will be able to detect relative brightness temperature variations of 0.1%, will provide strong constraints on the cutoff radius of the zonal winds.

3. Gravitational signals of deep zonal winds

Written in terms of density rather than entropy, the thermal wind balance also gives the density anomalies ρ' associated with a given zonal wind profile (Kaspi et al., 2010):

$$\nabla \rho' \times \mathbf{g} = (2\mathbf{\Omega} \cdot \nabla)[\tilde{\rho}\mathbf{u}]. \tag{11}$$
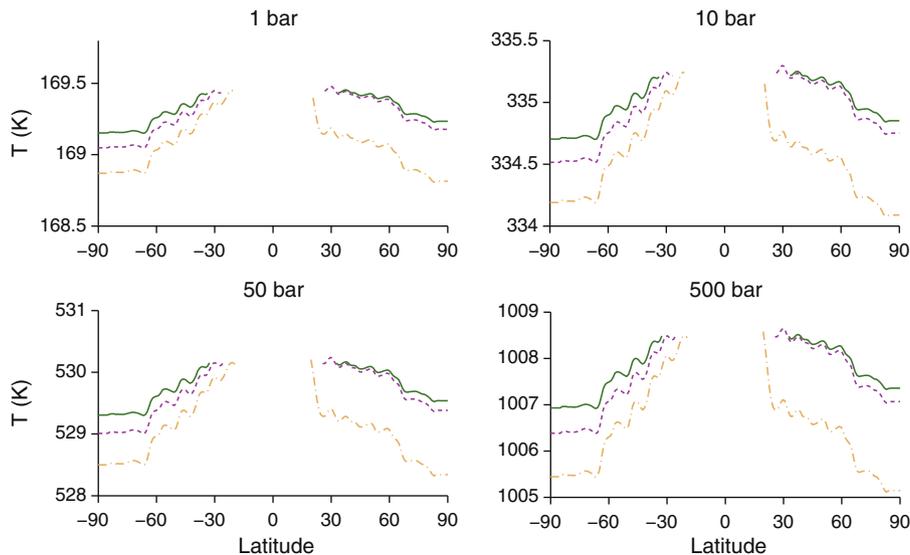

Fig. 5. Temperature perturbation as a function of latitude at different pressure levels. As in Fig. 3, green solid lines correspond to $r_c = 0.84R_J$, magenta dashed lines to $r_c = 0.90R_J$, and orange dash-dot lines to $r_c = 0.94R_J$. (For interpretation of the references to color in this figure legend, the reader is referred to the web version of this article.)
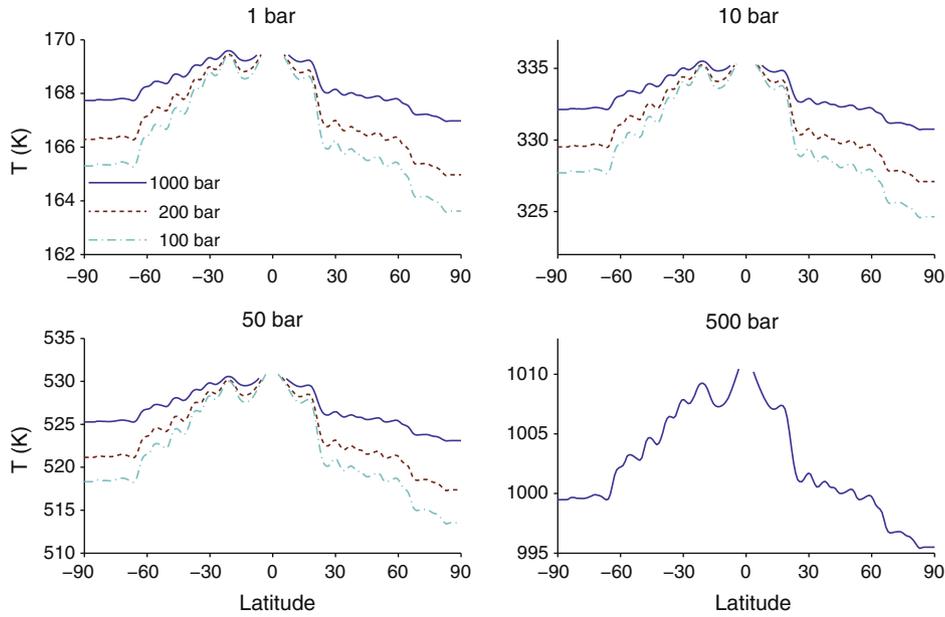
Fig. 6. Temperature perturbation as a function of latitude at different pressure levels for shallower cutoff radii. Deep blue solid lines correspond to $r_c = 0.9917R_J$ (corresponding to 1000 bar), brown dashed lines to $r_c = 0.9954R_J$ (200 bar), and light blue dash-dot lines to $r_c = 0.9965R_J$ (100 bar). (For interpretation of the references to color in this figure legend, the reader is referred to the web version of this article.)

The azimuthal component, now in spherical coordinates (r, ϕ), is

$$\frac{\partial \rho'}{\partial \phi} = \frac{2\Omega \cos \phi \, \tilde{\rho}}{g} \frac{\partial u}{\partial \phi} + \frac{2\Omega r \sin \phi}{g} \frac{\partial \tilde{\rho} u}{\partial r}, \qquad (12)$$

where the gravitational acceleration $g(r)$ continues to be a function of r. Using the SCVH EOS and assuming a hydrostatic reference state in which the reference density $\tilde{\rho}$ is only a function of spherical radius r, we can integrate the thermal wind equation along the meridional direction for any r and obtain the density perturbation for a given zonal wind distribution (Kaspi et al., 2010).[4]

The density anomaly ρ' perturbs Jupiter's gravity field through the perturbation of the gravitational potential

$$V(\mathbf{r}) = \frac{GM}{r} \left[1 - \sum_{n=2}^{\infty} \left(\frac{a}{r} \right)^n (J_n + \Delta J_n) P_n(\mu) \right]. \qquad (13)$$

Here, G is the gravitational constant, M is the planetary mass, $a = R_J$ is the planetary radius (taken at 1 bar), J_n is the zonal harmonic associated with the hydrostatic reference density distribution $\tilde{\rho}$ in solid body rotation, and ΔJ_n is the gravitational zonal harmonic associated with the density perturbation,

$$\Delta J_n = -\frac{1}{Ma^n} \int_0^a r'^{2+n} dr' \int_0^{2\pi} d\lambda' \int_{-1}^{1} P_n(\mu') \rho' d\mu', \qquad (14)$$

where $\mu' = \sin \phi$ and P_n is the Legendre polynomial of degree n. We consider the gravitational signals produced by equatorially symmetric zonal winds, which we take to be the winds obtained from the observed upper-tropospheric winds averaged between the northern and southern hemisphere. These are perturbations of the gravitational signals arising from the solid body rotation and also

from the oblateness of Jupiter, which we continue to neglect in the calculation of the perturbation zonal harmonics.[5]

Equatorially symmetric winds give rise to equatorially symmetric density perturbations and hence to even gravitational zonal harmonics ΔJ_n; odd zonal harmonics vanish. In the off-equatorial region, we calculate the winds based on (10), using the observed cloud-level zonal winds averaged between the northern and southern hemisphere as upper boundary condition $u_R(\phi)$. In the equatorial region outside the tangent cylinder (outside $r_\perp = r_c$), the zonal wind shear in the direction of the spin axis can vanish because cylinders concentric with the spin axis do not intersect the region of MHD drag at depth. We assume the equatorial winds penetrate unabatedly to the interior along the spin axis. As an example, Fig. 7 shows the density anomaly produced by such winds for the cutoff radius $r_c = 0.84R_J$. The density anomaly in the equatorial region is greater than that in the off-equatorial regions because equatorial wind speeds are greater. In the off-equatorial regions, the density anomaly is concentrated in the upper atmosphere due to the concentration of the wind shear there.

The corresponding even gravitational zonal harmonics ΔJ_n are shown in Fig. 8 for cutoff radii $r_c = 0.84R_J$, $0.94R_J$, $0.9917R_J$ (corresponding to 1000 bar), and $0.9965R_J$ (100 bar). For comparison, Fig. 8 also shows the zonal harmonics J_n of the reference state in solid body rotation (Hubbard, 1999), and the zonal harmonics ΔJ_n for zonal winds decaying very slowly with depth with scale height of 10^8 m (Kaspi et al., 2010). The magnitude of the zonal harmonics J_n of the reference state decreases rapidly with degree n; the magnitude of the perturbation zonal harmonics ΔJ_n associated with zonal winds is smaller for small n but does not decrease as rapidly for large n. Thus, to detect the even zonal harmonics

---

[4] In the calculation of the density perturbation from the thermal wind Eq. (12), an integration constant $\rho_0'(r)$ at each spherical radius r needs to be determined. Although this constant cannot be uniquely determined, we determine $\rho_0'(r)$ by the requirement that integrated over the sphere with radius r, the density perturbation vanishes, so that the perturbed state continues to satisfy in the mean the hydrostatic balance of the reference state with density $\tilde{\rho}$. Because in spherical geometry (which we assume), only the latitudinally varying part of the density affects the gravitational zonal harmonics (14), this choice of integration constant does not affect the zonal harmonics of interest to us here.

[5] Kong et al. (2012) calculated the gravity perturbations induced by deep zonal flows on a rapidly rotating oblate spheroid with constant density. According to their calculations, the gravitational zonal harmonics associated with the oblateness of the planet are much larger than those associated with the zonal flows for lower zonal harmonic degrees ($n < 6$). However, they are negligible for higher zonal harmonic degrees ($n \gtrsim 6$). Since the flattening of Jupiter is relatively small (1/16) and the gravitational zonal harmonics produced by zonal winds dominate over solid body rotation only for higher zonal harmonic degrees in any case [40], we neglect the gravity perturbation produced by the oblateness of Jupiter in this calculation.

Fig. 7. Density perturbation ρ' (kg m^{-3}) for cutoff radius $r_c = 0.84R_J$, calculated with the zonal winds averaged between the northern and southern hemisphere.

associated with zonal winds, Juno's gravity instrument has to detect signals of high degree n.

The zonal harmonics for deeper cutoff radii (0.84R_J and 0.94R_J) are about two orders of magnitude larger than those for a cutoff radius corresponding to 1000 bar, and about three orders of magnitude larger than those for a cutoff radius corresponding to 100 bar. For zonal winds with cutoff radii of 0.84R_J and 0.94R_J, and for zonal winds that are constant on cylinders (Hubbard, 1999), the zonal harmonics ΔJ_n start to be comparable in magnitude with the zonal harmonics J_n of the reference state at $n = 12$,

and they are significantly larger than J_n for $n \gtrsim 14$. For zonal winds with a cutoff radius corresponding to 1000 bar, the zonal harmonics ΔJ_n start to be comparable in magnitude with J_n at $n \gtrsim 14$; for even shallower zonal winds, the zonal harmonics ΔJ_n start to be comparable with J_n only at even higher $n \gtrsim 16$. These results are consistent with those of Kaspi et al. (2010), who found similar relations between the depths of the zonal winds and gravitational zonal harmonics by varying a specified exponential decay depth of the winds.

Juno's gravity instrument is expected to be able to detect gravitational zonal harmonics up to degree 12. Considering the possible noise in the data and the uncertainties in our model, it may be difficult for the gravity instrument to distinguish the effects of cutoff radii of 0.84 and 0.94R_J on the even zonal harmonics produced by equatorially symmetric zonal winds. It may also be difficult to distinguish our flow model from zonal winds that are decaying only slowly with depth (Kaspi et al., 2010). Measurement of the odd zonal harmonics produced by equatorially asymmetric zonal winds might help to distinguish different flow scenarios (Kaspi, 2013). Nonetheless, Juno's gravity instrument can be expected to be able to distinguish deep-flow scenarios (with cutoff radii as shallow as 0.94R_J) from shallow-flow scenarios (with cutoff radii corresponding to 1000 bar or less), which we consider implausible. If the gravity instrument were not to detect signals from deep zonal winds, the large meridional temperature variations associated with shallow zonal winds and their shear should be detectable by the microwave instrument.

Since the relation (12) between density perturbations and zonal wind perturbations and the decomposition (14) of the gravitational potential into zonal harmonics are linear, the perturbation zonal harmonic ΔJ_n can be further decomposed into a part associated with equatorial winds and a part associated with off-equatorial winds (inside the tangent cylinder with $r_\perp = r_c$). For deep cutoff radii (such as 0.84R_J), the gravitational signals produced by equatorial winds dominate (Fig. 9a). For shallower cutoff radii (such as
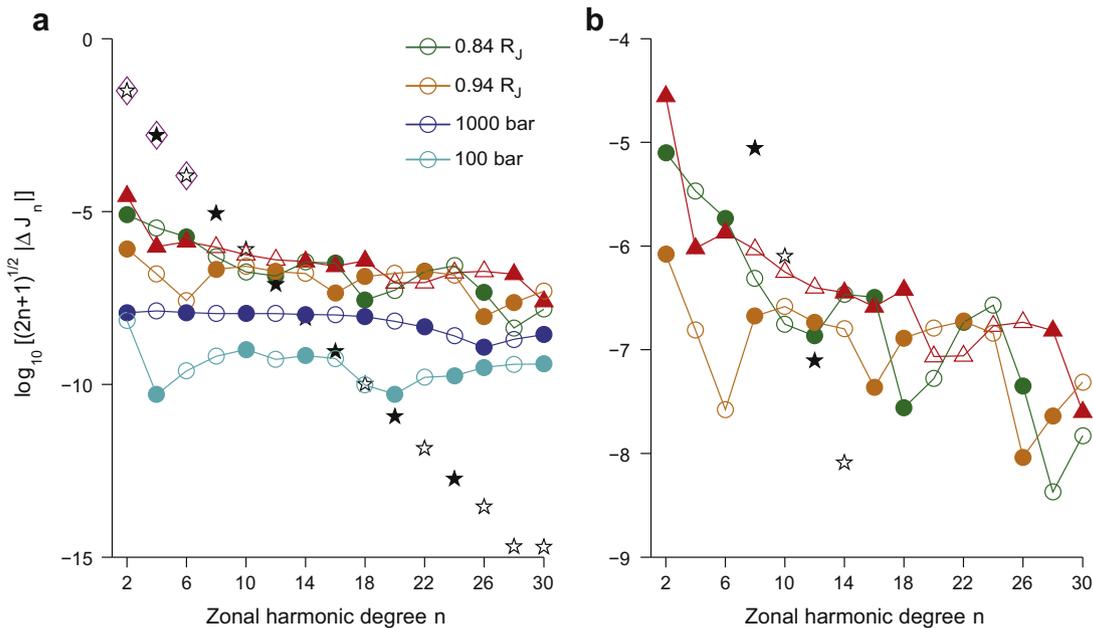

Fig. 8. Gravitational zonal harmonics associated with equatorially symmetric zonal winds. (a) Green circles/solid line: ΔJ_n for $r_c = 0.84R_J$. Orange circles/solid line: ΔJ_n for $r_c = 0.94R_J$. Deep blue circles/solid line: ΔJ_n for $r_c = 0.9917R_J$ (corresponding to 1000 bar). Light blue circles/solid line: ΔJ_n for $r_c = 0.9965R_J$ (corresponding to 100 bar). For comparison, the red triangles with dash-doted line show ΔJ_n for a model with zonal winds slowly decaying with depth with scale height of 10^8 m (Kaspi et al., 2010). Black stars shows the gravitational zonal harmonics of the reference state in solid body rotation (Hubbard, 1999), and magenta diamonds show observations from Voyager (Campbell and Synnott, 1985). Juno's gravity instrument is expected to be sensitive to zonal harmonics up to about degree 12. Filled (open) symbols indicate positive (negative) zonal harmonics. (b) Detailed comparison with enlarged y-axis. (For interpretation of the references to color in this figure legend, the reader is referred to the web version of this article.)
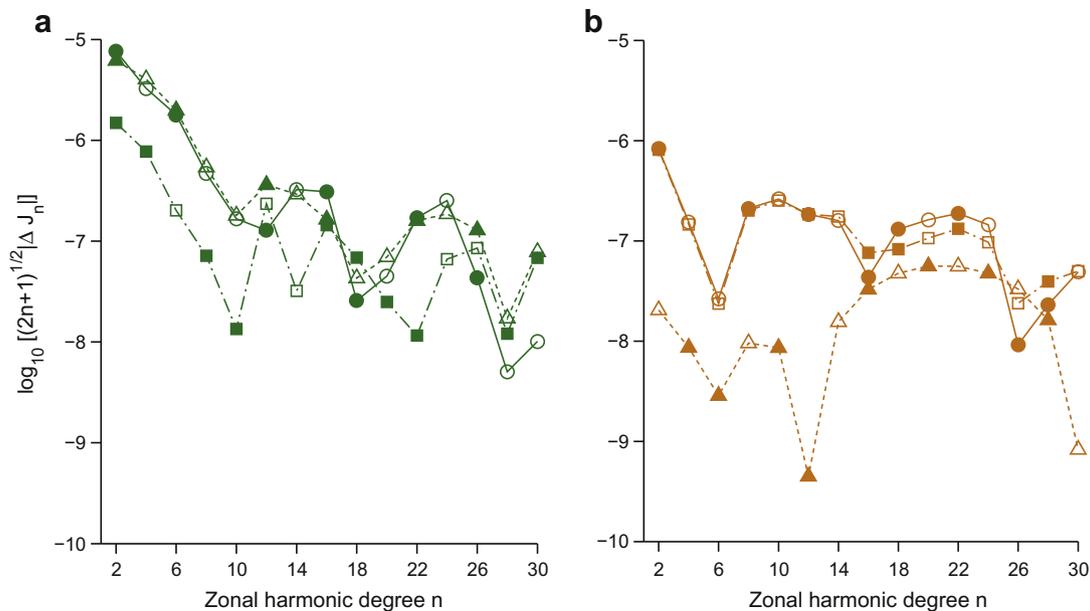
Fig. 9. Gravitational zonal harmonics associated with equatorially symmetric equatorial and off-equatorial zonal winds. Circles/solid line: zonal harmonics associated with equatorial and off-equatorial winds. Triangles/dashed line: zonal harmonics associated with equatorial winds. Squares/dash-dotted line: zonal harmonics associated with off-equatorial winds. (a) Cutoff radius $r_c = 0.84R_J$. (b) Cutoff radius $r_c = 0.94R_J$. Filled (open) symbols indicate positive (negative) zonal harmonics.

$0.94R_J$), the gravitational signals produced by the off-equatorial winds dominate. Therefore, if the cutoff radius is near the deeper end of what we consider plausible, it may be difficult for Juno to detect the gravity signal of deep off-equatorial zonal winds.

4. Conclusions

One of the main goals of the Juno mission is to measure the water and ammonia abundances in Jupiter's atmosphere below the visible clouds. To achieve this goal, Juno's microwave instrument is designed to measure the brightness temperature in six different channels sensitive to levels up to $O(100\ bar)$ (Janssen et al., 2005). However, the thermal signals measured by the microwave instrument come from two different sources: (i) opacity variations produced by variations in the water and ammonia abundances and (ii) temperature variations associated with zonal winds and their shear. Understanding the thermal signals of the zonal winds is crucial for accurately inferring the abundances of water and ammonia. We have shown that there exist strong physical constraints on the structure of the zonal winds, which constrain their thermal as well as their gravitational signals.

While it has long been assumed that entropy is completely homogenized in Jupiter's interior (Guillot et al., 2004), we have argued that—less restrictively—convection can only be expected to homogenize entropy along surfaces of constant angular momentum per unit mass, which are approximately cylinders concentric with the spin axis. Entropy gradients perpendicular to these surfaces then are constant going downward along the spin axis but cannot generally be zero for the flow to satisfy constraints derived from the angular momentum and energy balances. We have used this dynamical constraint on the interior entropy structure together with thermal wind balance to calculate zonal winds along with the temperature and density perturbations they imply. To do so, we had to assume a cutoff radius below which zonal winds are negligibly weak. Energetic arguments (that Ohmic dissipation associated with MHD drag at depth can at most be a fraction of the total energy available to drive the flow) and arguments based on the angular momentum balance (that the Maxwell stress must

be substantial below the cutoff radius) constrained plausible cutoff radii between $0.84R_J$ and $0.94R_J$. But because of uncertainties about the strength of the magnetic field at depth, uncertainties remain in these bounds for the cutoff radius (Appendices A and B).

Given our assumptions about the entropy structure, zonal winds and associated temperature and density perturbations can be calculated explicitly given a cutoff radius and an upper boundary condition. For the plausible cutoff radii between 0.84 and $0.94R_J$ and using the observed cloud-level winds as upper boundary condition, we calculated the zonal winds and the entropy, temperature, and density perturbations they imply. Because of the increase of density with depth and the equation of state of hydrogen, strong zonal winds and their shear are concentrated in the outer few percent of Jupiter's radius, irrespective of the precise value of the cutoff radius. Density variations associated with the zonal winds are also concentrated in Jupiter's outer layers. As a consequence, gravitational signals associated with zonal winds for different plausible cutoff radii may be difficult to distinguish. However, they are clearly different from gravitational signals associated with zonal winds confined above the 1000-bar level. Temperature variations associated with the zonal winds increase with depth. Equator-to-pole temperature contrasts reach ~1–2 K at 50 bar for plausible cutoff radii. This is well above the detection limit of Juno's microwave instrument. It is much larger than brightness temperature variations associated with plausible variations in water vapor abundance, but possibly smaller than brightness temperature variations associated with variations in ammonia abundance. Thus, Juno's gravity instrument can be expected to distinguish deep zonal winds from extremely shallowly confined zonal winds (which we consider implausible); its microwave instrument can be expected to provide constraints on the cutoff radius of deeper zonal winds provided variations in ammonia abundance can be further constrained by theory and modeling.

As an alternative to our physically based flow model, we have also considered consequences of a scenario in which zonal winds are confined above the 1000-bar level (outside $0.9917R_J$). In this case, gravitational signals of the zonal winds would likely not be detectable by Juno, but the equator-to-pole temperature contrasts would reach $O(10\ K)$ at 50 bar—a dynamical temperature signal

that would easily be detectable and would likely dominate meridional brightness temperature variations measured by the microwave instrument. Such extreme shallow-flow scenarios should be easily distinguishable from our more plausible deeper-flow scenario.

More generally, our dynamical constraints imply a structure of the zonal winds at depth that derives from a few straightforward and well justifiable assumptions. Calculation of the zonal winds at depth and of the entropy, temperature, and density perturbations they imply does not require a general circulation model, only evaluation of integrals, observations of zonal winds in the upper troposphere, and knowledge of the zeroth-order dynamical balances in the angular momentum equation (geostrophic) and in the radial momentum equation (hydrostatic). This wind structure and the associated temperature and density variations should provide strong constraints for inferring Jupiter's composition from measurements by the Juno mission.

Acknowledgments

Appendix A. Energetic constraints on depth of zonal winds

In the highly electrically conducting planetary interior, interactions of the flows with the magnetic field produce Ohmic dissipation. Detailed calculations of Ohmic dissipation produced by zonal winds have been provided by Liu et al. (2008). Here we give order of magnitude estimates relevant to the flows discussed in this paper.

The Ohmic dissipation per unit volume produced by the interaction of the magnetic field $\mathbf{B}$ with the flow $\mathbf{u}$ is given by

$$q = \frac{j^2}{\sigma}, \tag{A.1}$$

where σ is the electrical conductivity and j is the magnitude of the electric current $\mathbf{j} = \sigma(\mathbf{E} + \mathbf{u} \times \mathbf{B})$. If we neglect the effect of the electric field $\mathbf{E}$, the current scales like $j \sim UB$ (zonal velocity U and poloidal magnetic field strength B), and the Ohmic dissipation per unit volume can be estimated as

$$q \sim \sigma U^2 B^2. \tag{A.2}$$

Because the electrical conductivity is an exponential function of radius (Fig. 1a), the volume-integrated Ohmic dissipation Q mainly comes from the deepest layers with substantial zonal winds: a spherical shell extending about a scale height of the electrical conductivity H_σ outward from the cutoff radius r_c, so that

$$Q \sim 4\pi r_c^2 H_\sigma \sigma U^2 B^2. \tag{A.3}$$

Normalizing by the area of the sphere with radius R_J (to make the Ohmic dissipation directly comparable with the standard intrinsic and solar energy fluxes per unit area in the upper atmosphere), the Ohmic dissipation per unit area is

$$\widetilde{Q} \sim H_\sigma \sigma U^2 B^2 \left(\frac{r_c}{R_J} \right)^2. \tag{A.4}$$

The magnetic field strength B entering this dissipation estimate is uncertain. For example, the winds may nonlinearly modify the magnetic field. To evaluate the strength of the magnetic field, we use the dimensionless magnetic Reynolds number $R_m = UH_\sigma/\lambda$, where $\lambda = (\mu_0 \sigma)^{-1}$ is the magnetic diffusivity with magnetic permeability μ_0. The magnetic Reynolds number is the ratio of magnetic field generation to magnetic field dissipation. In Jupiter's outer layers where the electric conductivity of hydrogen is small enough, at depths with $R_m \lesssim 10$, the strength of the magnetic field can be estimated by downward continuation of the observed poloidal field in the upper atmosphere. In the deeper interior, at depths with $R_m \gtrsim 10$, magnetic field generation through dynamo action is strong and the field can be much stronger than observed in the upper atmosphere. If we take $U \sim 10$ m s^{-1} and $H_\sigma \sim 1000$ km, we obtain that $R_m \sim 10$ when the magnetic diffusivity is $\sim 1 \times 10^6$ m^2 s^{-1}, which occurs around $0.95R_J$. Thus, below $0.95R_J$, the magnitude of the magnetic field can be significantly greater than the observed outer field.

In the upper atmosphere, the observed poloidal magnetic field is $B_0 = 4.2$ Gauss (Connerney, 1993). If we continue this observed field downward, we have $B \sim B_0(R_J/r_c)^3$ at the cutoff radius r_c. For the Ohmic dissipation per unit area, this gives

$$\widetilde{Q} \sim H_\sigma \sigma U^2 B_0^2 \left(\frac{R_J}{r_c} \right)^4. \tag{A.5}$$

However, the dissipation per unit area is expected to be larger than this estimate at depth where $R_m \gtrsim 10$ because the downward continuation of the upper-atmospheric field underestimates the magnetic field strength at those depth.

Given the scale height of the electrical conductivity and a zonal velocity U near the cutoff radius, we can calculate an electrical conductivity $\sigma(r_c)$ (Fig. 1a) and the associated cutoff radius r_c at which the Ohmic dissipation per unit area $\widetilde{Q}$ begins to exceed a given threshold dissipation rate. For a threshold Ohmic dissipation of $\widetilde{Q} \sim 1$ W m^2 and $U \sim 10^{-2}$ m s^{-1}, this gives the threshold electrical conductivity of 1.25×10^5 S m^{-1} and $r_c \approx 0.84R_J$. If the magnetic field is an order of magnitude stronger than implied by the downward continuation of the upper-atmospheric field, zonal winds $U \sim 10^{-2}$ m s^{-1} would already experience a substantial dissipation of more than $\widetilde{Q} \sim 1$ W m^2 at $r_c \approx 0.89R_J$.

Additional uncertainties about the cutoff radius come from the fact that magnetic field lines at depth may align with the planetary spin axis, as seen in some dynamo simulations (Glatzmaier, 2008). Such alignment may reduce the Ohmic dissipation produced by the interaction of magnetic fields and zonal winds. However, this alignment can only occur where the magnetic Reynolds number R_m is much larger than unity, that is, within about $0.95R_J$ ($R_m \gtrsim 10$). If the magnetic field is perfectly aligned with the rotational axis inside a sphere with radius r_*, and is taken to be a potential field outside of r_*, the surface current at r_* still generates significant Ohmic dissipation, even when the Ohmic dissipation inside the spherical radius r_* is reduced (Liu et al., 2008). Thus, to avoid generating excessive Ohmic dissipation, the magnitude of the flow at r_* must be weak. Given that r_* must be in a region of large magnetic Reynolds number and thus within about $0.95R_J$, these additional complications arising from nonlinear interactions with the magnetic field do not substantially affect the uncertainty bracket for the cutoff radius we have given.

Appendix B. Maxwell stress

In the region with significant electrical conductivity, the thermal wind equation breaks down and zonal wind shear along the spin axis is primarily determined by the Maxwell stress produced by the planetary magnetic field:

$$\frac{\partial u}{\partial z} \approx \frac{1}{2\Omega\mu_0} \left[\nabla \times \left(\frac{\overline{(\nabla \times \mathbf{B}) \times \mathbf{B}}}{\bar{\rho}} \right) \right] \cdot \mathbf{e}_\lambda. \tag{B.1}$$

Here, $\mathbf{e}_\lambda$ is the unit vector in the zonal direction. The magnitude of the (dimensionless) zonal wind shear along the spin axis resulting from the Maxwell stress can estimated as (Eq. (33) in Liu et al. (2008))

$$\left|\frac{H_\rho}{U}\frac{\partial u}{\partial z}\right| \sim \frac{F\mu_0\sigma}{2\Omega U\tilde{\rho}}, \tag{B.2}$$

where H_ρ is the typical scale for the zonal velocity variation along the spin axis, F is the planetary internal heat flux, and σ is the electrical conductivity. The Maxwell stress becomes significant when the estimated dimensionless zonal wind shear reaches unity.

Liu et al. (2008) estimated the zonal wind shear produced by the Maxwell stress at the maximum penetration depth ($0.96R_J$) for zonal winds that are constant along the spin axis. The calculated dimensionless zonal wind shear is about 10^{-5}, which implies that the Maxwell stress is not large enough to influence the zonal wind shear along the spin axis if the observed zonal winds penetrate to the planetary interior unabatedly.

However, as we discussed in Section 2.2, the zonal winds generally must be sheared along the spin axis even in the upper atmosphere, where Maxwell stresses are insignificant. Their magnitudes, away from the equatorial regions, generally can be expected to decrease toward the interior (Fig. 2). As a consequence, sheared zonal winds with diminishing magnitude can penetrate deeper into the planetary interior without violating Ohmic dissipation constraints, and Maxwell stresses may substantially affect the zonal wind shear. If we take $\Omega \sim 1.76 \times 10^{-4}\,\text{s}^{-1}$, $\tilde{\rho}$ as the density in the interior of Jupiter calculated from SCVH EOS (for example, $\tilde{\rho} \sim 200\,\text{kg m}^{-3}$ at $0.94R_J$), the dimensionless zonal wind shear reaches unity for a zonal wind magnitude of $10^{-2}\,\text{m s}^{-1}$ at the region with $\sigma \sim 50\,\text{S m}^{-1}$, corresponding to $0.94R_J$. At or below $0.94R_J$, the thermal wind equation breaks down and the zonal wind shear along the spin axis is determined by the Maxwell stress. Thus, the depth of $0.94R_J$ provides an estimate for the upper bound of the cutoff radius.

References

Atkinson, D.H., Ingersoll, A.P., Seiff, A., 1997. Deep winds on Jupiter as measured by the Galileo probe. Nature 388, 649–650.

Atkinson, D.H., Pollack, J.B., Seiff, A., 1998. The Galileo probe Doppler wind experiment: Measurement of the deep zonal winds on Jupiter. J. Geophys. Res. 103, 22911–22928.

Aurnou, J., Heimpel, M., Allen, L., King, E., Wicht, J., 2008. Convective heat transfer and the pattern of thermal emission on the gas giants. Geophys. J. Int. 173, 793–801.

Busse, F.H., 1976. A simple model of convection in the jovian atmosphere. Icarus 29, 255–260.

Busse, F.H., 1994. Convection driven zonal flows and vortices in the major planets. Chaos 4, 123–134.

Campbell, J.K., Synnott, S.P., 1985. Gravity field of the jovian system from Pioneer and Voyager tracking data. Astrophys. J. 90, 364–372.

Christensen, U.R., 2001. Zonal flow driven by deep convection in major planets. Geophys. Res. Lett. 28, 2553–2556.

Connerney, J.E.P., 1993. Magnetic fields of the outer planets. J. Geophys. Res 98 (E10), 18659–18679.

Emanuel, K.A., 1983. On assessing local conditional symmetric instability from atmospheric soundings. Mon. Wea. Rev. 111, 2016–2033.

Emanuel, K.A., 1994. Atmospheric Convection. Oxford University Press, New York.

French, M. et al., 2012. Ab initio simulations for material properties along the Jupiter adiabat. Astrophys. J. 202 (Suppl.), 5.

Gastine, T., Wicht, J., 2012. Effects of compressibility on driving zonal flow in gas giants. Icarus 219, 428–442.

Gierasch, P.J. et al., 2000. Observation of moist convection in Jupiter's atmosphere. Nature 403 (6770), 628–630.

Glatzmaier, G.A., 2008. A note on "Constraints on deep-seated zonal winds inside Jupiter and Saturn". Icarus 196, 665–666.

Guillot, T., 1999. A comparison of the interiors of Jupiter and Saturn. Planet. Space Sci. 47, 1183–1200.

Guillot, T., 2005. The interiors of giant planets: Models and outstanding questions. Ann. Rev. Earth Planet. Sci. 33, 493–530.

Guillot, T., Morel, P., 1995. CEPAM: A code for modeling the interiors of giant planets. Astron. Astrophys. 109 (Suppl. Ser.), 109–123.

Guillot, T., Stevenson, D.J., Hubbard, W.B., Saumon, D., 2004. The interior of Jupiter. In: Bagenal, F., Dowling, T.E., McKinnon, W.B. (Eds.), Jupiter: The Planet, Satellites and Magnetosphere. Cambridge University Press, pp. 35–57.

Heimpel, M., Gómez Pérez, N., 2011. On the relationship between zonal jets and dynamo action in giant planets. Geophys. Res. Lett. 38, L14201.

Heimpel, M., Aurnou, J., Wicht, J., 2005. Simulation of equatorial and high-latitude jets on Jupiter in a deep convection model. Nature 438 (7065), 193–196.

Hubbard, W.B., 1999. Gravitational signature of Jupiter's deep zonal flow. Icarus 137, 357–359.

Ingersoll, A.P. et al., 2004. Dynamics of Jupiter's atmosphere. In: Bagenal, F., Dowling, T.E., McKinnon, W.B. (Eds.), Jupiter: The Planet, Satellites and Magnetosphere. Cambridge University Press, pp. 105–128.

Ingersoll, A.P., Cuzzi, J.N., 1969. Dynamics of Jupiter's cloud bands. J. Atmos. Sci. 26, 981–985.

Ingersoll, A.P., Pollard, D., 1982. Motions in the interiors and atmospheres of Jupiter and Saturn: Scale analysis, anelastic equations, barotropic stability criterion. Icarus 52, 62–80.

Ingersoll, A.P., Porco, C.C., 1978. Solar heating and internal heat flow on Jupiter. Icarus 35, 27–43.

Ingersoll, A.P., Beebe, R.F., Mitchell, J.L., Garneau, G.W., Yagi, G.M., Müller, J.-P., 1981. Interaction of eddies and mean zonal flow on Jupiter as inferred from Voyager 1 and 2 images. J. Geophys. Res. 86, 8733–8743.

Janssen, M.A., Hofstadter, M.D., Gulkis, S., Ingersoll, A.P., Allison, M., Bolton, S.J., Levin, S.M., Kamp, L.W., 2005. Microwave remote sensing of Jupiter's atmosphere from an orbiting spacecraft. Icarus 173, 447–453.

Jones, C., Kuzanyan, K.M., 2009. Compressible convection in the deep atmospheres of giant planets. Icarus 204, 227–238.

Kaspi, Y., Flierl, G.R., Showman, A.P., 2009. The deep wind structure of the giant planets: Results from an anelastic general circulation model. Icarus 202, 525–542.

Kaspi, Y., Hubbard, W.B., Showman, A.P., Flierl, G.R., 2010. Gravitational signature of Jupiter's internal dynamics. Geophys. Res. Lett. 37, L01204.

Kaspi, Y., 2013. Inferring the depth of the zonal jets on Jupiter and Saturn from odd gravity harmonics. Geophys. Res. Lett. 40, http://dx.doi.org/10.1029/2012GL053873.

Kong, D., Zhang, K., Schubert, G., 2012. On the variation of zonal gravity coefficients of a giant planet caused by its deep zonal flows. Astrophys. J. 748, 143–151.

Limaye, S.S., 1986. Jupiter: New estimates of the mean zonal flow at the cloud level. Icarus 65, 335–352.

Liu, J.J., 2006. Interaction of the Magnetic Field and Flow in the Outer Shells of Giant Planets. Caltech Thesis.

Liu, J.J., Schneider, T., 2010. Mechanisms of jet formation on giant planets. J. Atmos. Sci. 67, 3652–3672.

Liu, J.J., Goldreich, P.M., Stevenson, D.J., 2008. Constraints on deep-seated zonal winds inside Jupiter and Saturn. Icarus 196, 653–664.

Magalhães, J.A., Seiff, A., Young, R.E., 2002. The stratification of Jupiter's troposphere at the Galileo probe entry site. Icarus 158, 410–433.

Nellis, W.J., Mitchell, A.C., McCandless, P., Erskine, D.J., Weir, S.T., 1992. Electronic energy gap of molecular hydrogen from electrical conductivity measurements at high shock pressures. Phys. Rev. Lett. 68 (19), 2937–2940.

Nellis, W.J., Weir, S.T., Mitchell, A.C., 1996. Metallization and electrical conductivity of hydrogen in Jupiter. Science 273 (5277), 936–938.

Pedlosky, J., 1987. Geophysical Fluid Dynamics, second ed. Springer, New York.

Porco, C.C. et al., 2003. Cassini imaging of Jupiter's atmosphere, satellites, and rings. Science 299 (5612), 1541–1547.

Russell, C.T., Yu, Z.J., Khurana, K.K., 2001. Magnetic field changes in the inner magnetosphere of Jupiter. Adv. Space Res. 28, 897–902.

Salyk, C., Ingersoll, A.P., Lorre, J., Vasavada, A., Del Genio, A.D., 2006. Interaction between eddies and mean flow in Jupiter's atmosphere: Analysis of Cassini imaging data. Icarus 185 (2), 430–442.

Sánchez-Lavega, A. et al., 2008. Depth of a strong jovian jet from a planetary-scale disturbance driven by storms. Nature 451, 437–440.

Saumon, D., Chabrier, G., Van Horn, H., 1995. An equation of state for low-mass stars and giant planets. Astrophys. J. 99, 713–741.

Schneider, T., Liu, J.J., 2009. Formation of jets and equatorial superrotation on Jupiter. J. Atmos. Sci. 66, 579–601.

Seiff, A. et al., 1998. Thermal structure of Jupiter's atmosphere near the edge of a 5-μm hot spot in the north equatorial belt. J. Geophys. Res. 103 (E10), 22857–22889.

Smith, B.A., Soderblom, L., Batson, R., Bridges, P., Inge, J., Masursky, H., Shoemaker, E., Beebe, R., Boyce, J., Briggs, G., Bunker, A., Collins, S.A., Hansen, C.J., Johnson, T.V., Mitchell, J.L., Terrile II, R.J., Cook, A.F., Cuzzi, J., Pollack, J.B., Danielson, G.E., Ingersoll, A.P., Davis, M.E., Hunt, G.E., Morrison, D., Owen, T., Sagan, C., Veverka, J., Strom, R., Suomi, V.E., 1982. A new look at the saturn system: The Voyager 2 images. Icarus 215, 504–537.

Thorpe, A.J., Rotunno, R., 1989. Nonlinear aspects of symmetric instability. J. Atmos. Sci. 46, 1285–1299.

Vallis, G.K., 2006. Atmospheric and Oceanic Fluid Dynamics: Fundamentals and Large-Scale Circulation. Cambridge University Press, Cambridge, UK.